FULL PAPER

Interface Driven Pseudo-Elasticity in α-Fe Nanowires

Yang Yang, Suzhi Li,* Xiangdong Ding,* Jun Sun, and Ekhard K. H. Salje*

Molecular dynamics simulations of bent [100] α-Fe nanowires show the nucleation of twins and nanoscale interfaces that lead to pseudo-elasticity during loading/unloading cycles. The new type of interfaces along {110} stems from the accumulation of individual <111>/{112} twin boundaries and stores high interfacial energies. These nonconventional interfaces provide a large part of the driving force for shape recovery upon unloading, while the minimization of surface energy is no longer the dominant driving force. This new pseudo-elastic effect is not much affected by surface roughness, and can be extended over a wide range of wire diameters, if the sample is seeded with conventional twin boundaries, which will transform to the desired {110} interfaces under bending.

1. Introduction

Fe based nanowires are the key element in magnetic racetrack technologies for high density memory devices.[1] In this application, mobile domain walls and interfaces are the carriers of information. Magnetoresistance (MR) measurements as functions of domain wall density, temperature, and angle of the applied field determine the field MR contributions. They relate to conventional ferromagnetism and the erasure of domain walls. A negative domain wall contribution to the resistivity shows that domain boundaries are an important hindrance for electronic transport while electron transport in Fe micro or nanowires without such domain structures is particularly large.[2] In racetrack technologies, magnetic domain walls are generated during the writing action. These walls often interact with low-velocity domain walls such as twin walls, which is detrimental for the device performance.[3,4] The understanding of twin walls and other domain walls are hence crucial for the optimization of nanowires for racetrack-type memory devices. We will specify exactly the conditions under which the formation of nanostructures is reversible after bending the nanowire.

Dr. Y. Yang, Dr. S. Z. Li, Prof. X. Ding,
Prof. J. Sun, Prof. E. K. H. Salje
State Key Laboratory for Mechanical
Behavior of Materials
Xi'an Jiaotong University
Xi'an 710049, China
E-mail: lsuzhi@gmail.com; dingxd@mail.xjtu.edu.cn;
ekhard@esc.cam.ac.uk
Prof. E. K. H. Salje
Department of Earth Sciences
University of Cambridge
Cambridge CB2 3EQ, UK

Reversibility is typically related to the shape memory effect and pseudo-elasticity in shape memory alloys (SMAs).[5–7] The shape recovery is achieved by thermoelastic martensitic phase transformations and domain switching. The driving force for the shape recovery arises from the free energy difference between the martensite and parent phase. This effect is strongly size-dependent and it is not obvious how SMAs operate in thin wires.[8,9] The fundamental question is whether a different shape memory effect exists at the nanoscale and if so by which mechanism. This is important because many traditional SMAs fail under nanoscale bending and it becomes important to search for alternative functional materials to replace the traditional SMAs for such nanoscale applications. We show by molecular dynamics simulations that α-Fe, which is not a shape memory alloy, also shows shape recovery (or pseudo-elasticity) after bending. Large bending in α-Fe occurs via the formation of interfaces between domains of different orientation and twinning. The deformed nanowire completely recovers under unloading. The mechanism is shown to be very different from the classic pseudo-elasticity, and is related to high-energy interfaces in the nanowire and not the martensite-austenite phase transformation. This result has implications more widely for shape-dependent SMAs that are used in microelectromechanical systems (MEMS) technology. This is also an example of the emerging field of domain boundary engineering where functionality (namely the shape recovery) is linked to domain boundaries and interfaces, but not to bulk properties (such as the martensite–austenite phase transformation).[10–12]

Previous molecular dynamics (MD) simulations have identified a class of metallic nanowires with both face-centered cubic (fcc) and body-centered cubic (bcc) structures that show pseudo-elasticity and shape memory effects.[13–19] This pseudo-elastic behavior was achieved under uniaxial tension while little is known whether such unique behavior can still exist when a wire is bent. Under tension, the shape recovery relates to the reversibility of conventional twinning. The driving force for the recoverable deformation stems from the minimization of the surface energy.[14,15,17,18] The total recoverable strain is very large and can exceed 40%. A large inelastic deformation mediated by conventional twinning has been confirmed experimentally in fcc palladium and bcc tungsten.[20,21] Here we also show that the shape recovery effect under bending in α-Fe relates to the formation of nonconventional interfaces between domains of different orientations. Unlike conventional <111>/{112}-type

www.MaterialsViews.com

ADVANCED
FUNCTIONAL
MATERIALS
www.afm-journal.de

FULL PAPER

twinning in bcc metal, these interfaces under bending lie in {110} planes of α-Fe and possess high interfacial energies. The nanowire completely recovers after unloading. The thermodynamic driving force is hence very different from the pseudo-elasticity in bcc and fcc nanowire under tension, as it is related to high-energy interfaces, while the surface energy becomes somewhat less important. We also show that this bending induced pseudo-elasticity can be extended to a wide range of wire diameters if the sample is seeded with conventional twin boundaries, which will transform to the desired {110} interfaces under bending.

2. Results and Discussion

2.1. Bending Induced Pseudo-Elasticity

Bending is achieved by tilting the rigid loading ends against each other, while keeping the neutral line constant (**Figure 1**a). The bending angle θ is defined as half of the inclination angle of the two fixed surface layers against each other (parallel surfaces layers for $\theta = 0°$ and semi-circle bending for $\theta = 90°$). The bending deformation generates a stress gradient as shown in Figure 1b. The magnitude of stress normal to the cross-sectional area drops linearly from a tensile stress at the top surface to a compressive stress at the bottom surface. The bending moment is calculated by integrating the moments of all atomic sites in the cross-sectional area as $\int_S \sigma_n l \, dS$, where σ_n is the normal stress for each atomic site in the loading grid, l is the distance from the atomic site to the neutral line and S is the cross-sectional area of the loading grid.

Figure 2a shows the bending moment as a function of bending angle at 300 K in a α-Fe nanowire with dimensions 22.6 nm × 3.2 nm × 3.2 nm. The black and red curves refer to loading and unloading stages, respectively. The nanowire first undergoes an elastic deformation under loading with an almost linear increase of the bending moment and then yields when $\theta = 22°$. The bending moment undergoes an abrupt drop at the yield point; further yield events follow at higher bending angles. The nanowire is then unloaded from the maximum bending angle of 80°. After unloading, the nanowire fully recovers its original shape (red curve in Figure 2a).

The atomic configurations during the (un-)bending process show recovery/nucleation of domains and interfaces. Figure 2b–i shows the atomic configurations during loading and unloading. Starting from the pristine nanowire (Figure 2b), interfaces nucleate from the top surface when the nanowire first yields (Figure 2c). Bending produces a large tensile stress in the top surface where twin planes nucleate. These planes are

the conventional <111>/{112}-type twin planes as reported for [100]-oriented α-Fe nanowire under tension.[14] Once interfaces and domains nucleate, they grow towards the inside of the nanowire in a wedge shape (Figure 2d). Further loading nucleates more domains and promotes their growth (Figure 2e,f). The interfaces layer of the triangular domain is distorted and lies near the {110} plane instead of the conventional {112} twin plane in bcc crystals. The nucleation and growth of twin regions correspond to the change of the bending moment in Figure 2a.

A recoverable detwinning process occurs when the nanowire is unloaded, as shown in Figure 2g–i. The increase of bending moment in Figure 2a corresponds to the detwinning progress. The annihilation of domains is accomplished at $\theta = 17°$. Further unloading leads to the release of elastic energy. Note that we avoided the intersections between twins and the wire-surface at the lowest layer because such intersections induce major disruptions during the shape recovery to the sample.

2.2. The Nonconventional {110}-Type Interface

Figure 3a shows the morphology of the {110} interface in a side view at $\theta = 26°$. The top four layers of the nanowire are shown in different colors. A red dashed circle marks the nucleation site of the triangle-shaped interface. Figure 3b shows the atomic arrangement in the [011] direction of the highlighted area. Figure 3c–f shows the atomic arrangement of each plane from the inside to the top surfaces: a local <111>/{112} "twin" forms in each layer whereby the "twin plane" of each layer glides like a $a/6$ [11$\bar{1}$] partial dislocation. The thicknesses of the local <111>/{112} twin in each layer are not constant but decrease from the top layer downwards. In fact, we find no twinning in the fourth layer in Figure 3c while there is still a weak displacement in the third layer. The $a/6$ [11$\bar{1}$] partial dislocation nucleates from the surface and glides in the plane, leading to a lattice misfit in this layer as indicated in the grey solid line in Figure 3d–e. The displacement of atoms near the surface becomes larger than that in the interior of the wire, e.g., the displacements in the second layer are twice as large as the $a/6$ partial (Figure 3e) and the displacements in the first layer increase to three times of the $a/6$ partial (Figure 3f). The relative displacement persists between each adjacent layers and thus shows that the {110} interface is formed by piling up a series of local <111>/{112} twins. Here we can see that the configuration of the nonconventional {110} interface is quite different from the <111>/{112} twin boundary. A schematic image of the formation of traditional <111>/{112} twins and non-conventional {110} interfaces is shown in Figure S1 (Supporting Information).
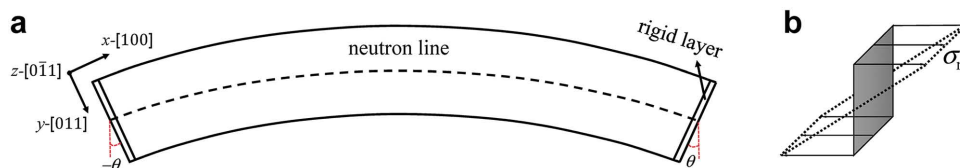

Figure 1. Illustration of bending deformation in nanowires. a) Simulation model. b) Distribution of normal stress in cross-sectional area.
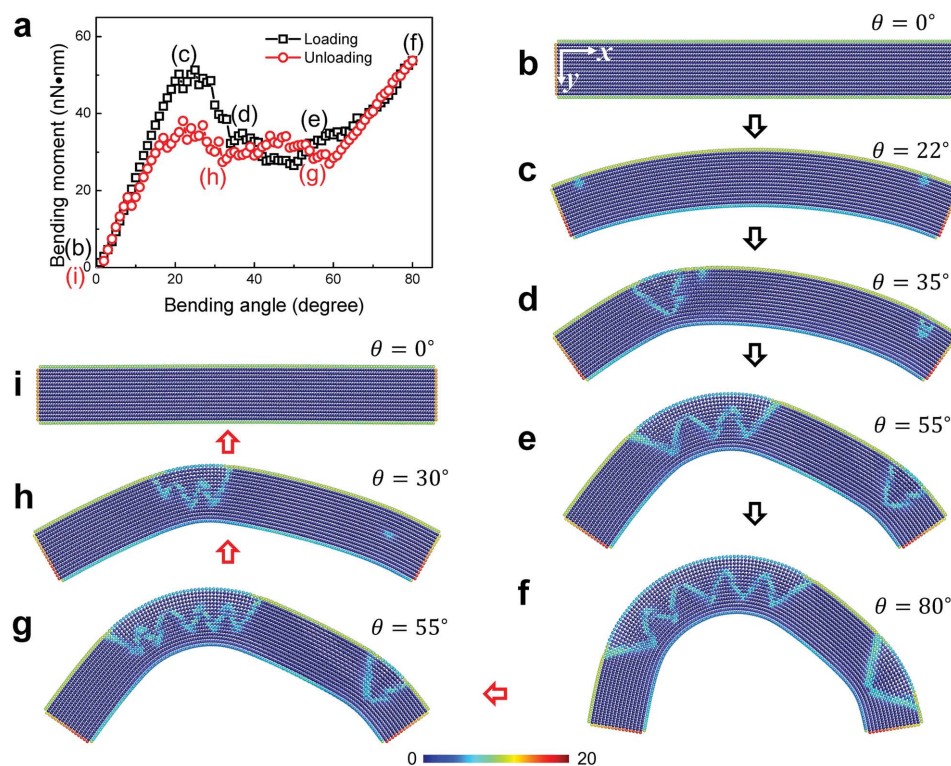
**ADVANCED
FUNCTIONAL
MATERIALS**

www.afm-journal.de

FULL PAPER

*Materials
Views*

www.MaterialsViews.com

Figure 2. Pseudo-elasticity of α-Fe nanowire (22.6 nm × 3.2 nm × 3.2 nm) under bending at 300 K. a) The variation of bending moment with bending angle. b–f) Typical atomic images for loading. g–i) Typical atomic images for unloading. The color of the atoms represents the centrosymmetry parameter.[22]
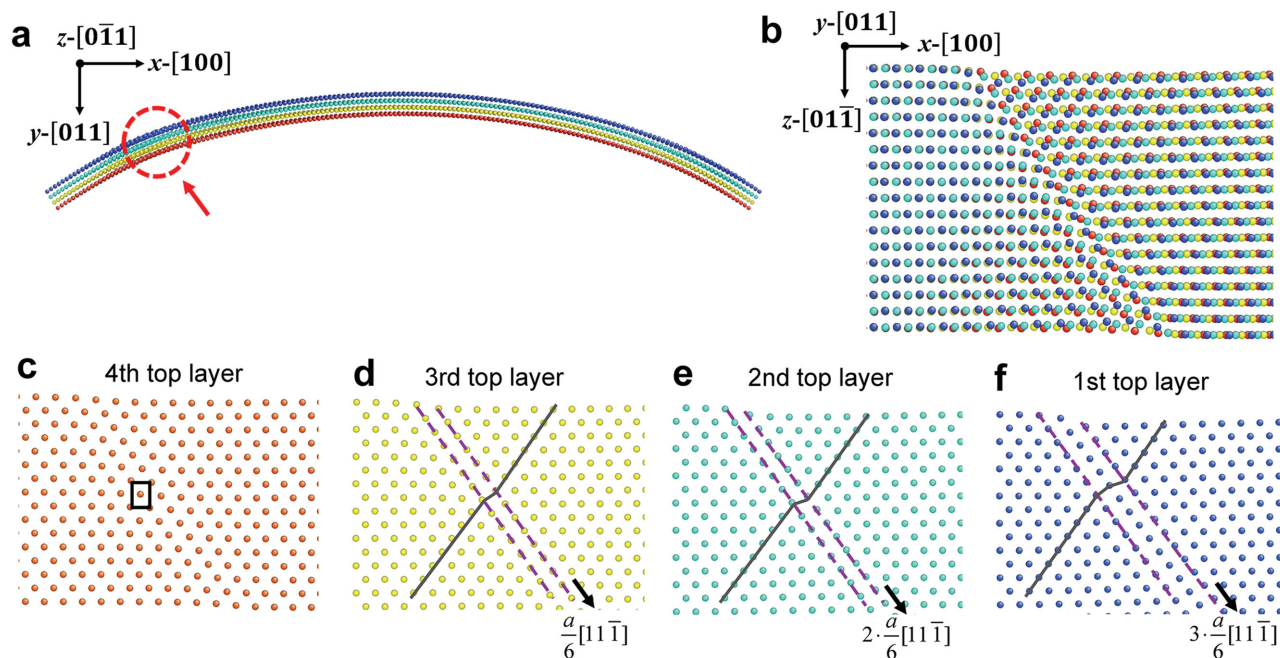

Figure 3. Illustration of a distorted {110} interface. a) The snapshot of deformed nanowires at $\theta = 26°$. The top four layers are present for each layer in a different color. The area indicated by the arrow is where the {110} interface forms. b) Top view of atomic configuration in the area indicated by the arrow. c–f) Atomic images for each top single layer from inside to the top of the nanowire.
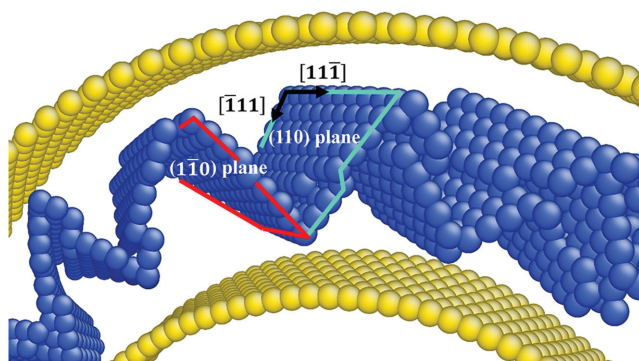
www.MaterialsViews.com

ADVANCED
FUNCTIONAL
MATERIALS
www.afm-journal.de

FULL PAPER

Figure 4. Snapshot of a {110} interface under bending. The morphology of the {110} interface is typically W-shaped.

Once nucleated, further bending induces the growth of the {110} interface. **Figure 4** shows the atomic configuration of interfaces in a highly deformed nanowire. The atoms in yellow color indicate the surfaces and those in blue color refer to the {110} layer of the interface. All local twin boundaries are distorted and connected to form a W shape with each segment in the {110} planes. In fact, W-shaped interfaces are similar to bifurcated twins and commonly observed in ferroelastic materials.[23,24]

2.3. The Effect of the Surface Roughness on Pseudo-Elasticity

Present experimental techniques can fabricate nanowires of ultrathin size,[25,26] approaching that of our simulations. However, it is very difficult to produce materials without any defects and dislocations. Surface roughness and vacancies will always exist. In order to mimic the experimental conditions, we analyze the effect of preexisting defects on the pseudo-elastic behavior. The density of preexisting dislocations is usually very low, as the nanowire is in the "dislocation starvation" state.[27]

Here we primarily consider the effect of the surface roughness on the twinning deformation and the related pseudo-elasticity.

A rough surface was created by removing surface atoms randomly from a pristine nanowire. **Figure 5**a shows the initial model with 5% of the surface atoms removed. The nanowire was then subjected to the same loading/unloading experiment as the perfect wire. We find that the surface roughness does not have a significant influence on the twinning mediated pseudo-elasticity. The variation of the bending moment as function of the bending angle is shown in Figure 5b and behaves similarly as that in the smooth nanowires. Twinning is still the dominant mode under bending deformation, as shown in Figure 5c–f. The {110} interfaces and W-shaped patterns are formed. The detwinning progress occurs at the unloading stage and the shape of the nanowire is almost completely recovered after unloading.

Surface roughness is hence relatively unimportant for bending deformations in nanoscale α-Fe wires when twinning is the main deformation mechanism. This is different from macroscopic bcc crystals, such as α-Fe, W, and Mo, where plastic strain is primarily carried by dislocations and deformation twinning is less common.[28] However, when the size reduces from the micro to the nanoscale, the material strength increases dramatically,[29–31] and dislocations become rare.[32,33] Previous simulations and experiments on nanoscale α-Fe under tension already showed that twinning dominates.[34–38]

2.4. Multitwinned Bending Pseudo-Elasticity Based Nonconventional {110} Interfaces

Our results apply only to very thin nanowires. When we upscale the size of the nanowire, dislocations will appear during deformation, which potentially destroys pseudo-elasticity. To avoid the nucleation of dislocations, we seed the sample with conventional <111>/{112} twin boundaries. These twin boundaries are expected to become non-conventional {110}-type interfaces
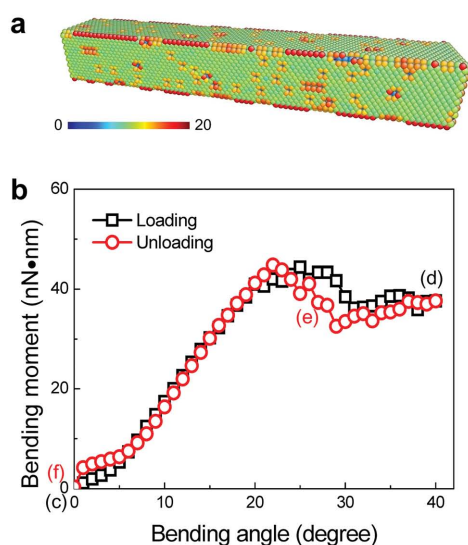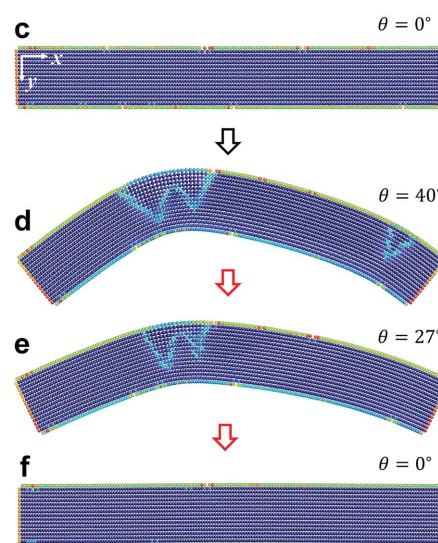

Figure 5. The effect of surface roughness on pseudo-elasticity. a) The initial configuration of nanowires with rough surfaces. The color of the atoms is shown according to its centrosymmetry parameter.[22] b) The variation of bending moment with bending angle. c–f) Atomic configurations marked in (b).

**ADVANCED
FUNCTIONAL
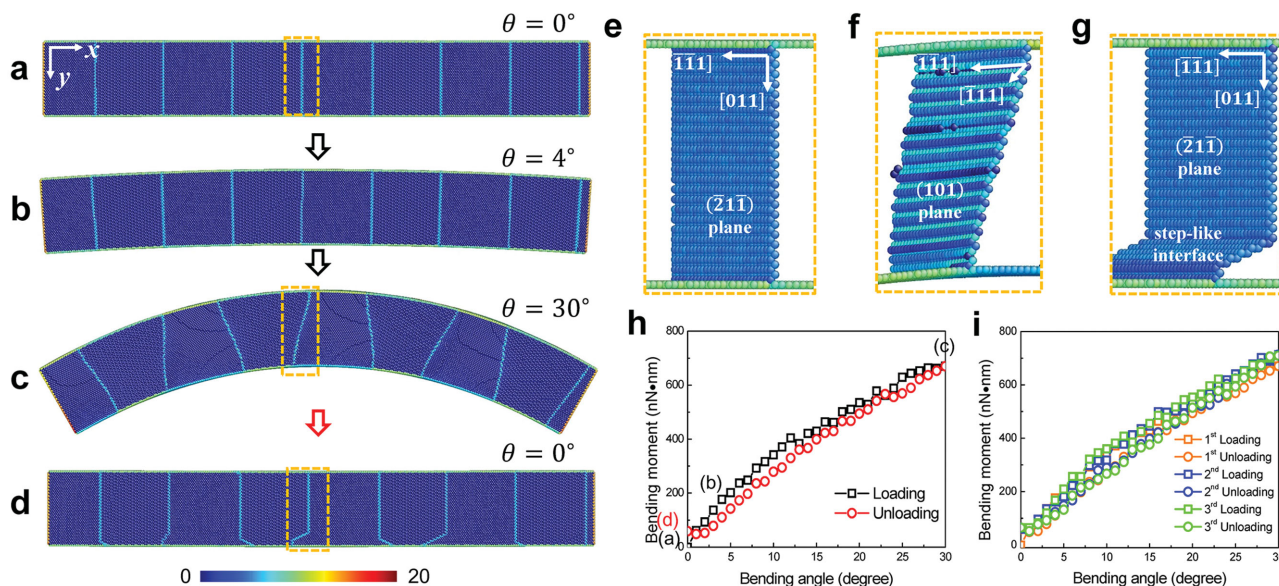MATERIALS**

www.afm-journal.de

Materials Views

www.MaterialsViews.com

Figure 6. The bending of a <111>/{112} multi-twinned nanowire. a–d) Typical atomic images for loading and unloading. e–g) The interface morphology of different types in details. h) The variation of bending moment with bending angle in the first bending cycle. i) The variation of bending moment with bending angle in the first three bending cycles. The pseudo-elastic effect was fully recoverable under multiple cycling (after the first cycle when some defects were generated near the lower surface). The color of the atoms show their centrosymmetry parameter.[22]

under bending, as shown in **Figure 6**. Once the sample is seeded with twin boundaries, we find that no dislocations nucleate because the preexisting twin boundaries compensate the main part of the bending energy. Seeding is hence the second "defect mechanism," which turns out to be beneficial for shape recovery.

In the simulations, we consider a nanowire with a multi-domain structure. The initial dimension of wire is 72 nm in x-[100], 10 nm in y-[011] and z-[0$\bar{1}\bar{1}$] directions, respectively. The twin spacing is ≈8 nm. The sample was then bent in the xy-plane. Figure 6b–d shows the shape of the nanowire upon loading/unloading of a multitwinned sample. The pre-existing twin boundaries first lie in {112} planes (Figure 6e). They start to move when the bending angle reaches 4°, after the end of the elastic regime. Twin planes bend by generating steps in the interface. In this way the {112} twin boundary transforms to the {110} interface (Figure 6f). Most of the {110} interfaces transform back to the original {112} twin boundaries upon unloading. However, we noticed that some step-like interfaces are formed near the bottom surface when the bending angle reaches zero (Figure 6g). Figure 6h shows the variation of the bending moment with bending angle during the loading/unloading process. The unloaded nanowire contains some steps and does, therefore, not completely transform back to the original state after the first unloading. Nevertheless, the remaining defects do not change the fundamental process of pseudo-elasticity. During the second and third cyclic bending deformation, the nanowire continues with full shape recovery behavior. The "defect" region is already present in the initial state (after the first cycle) of the shape recovery experiment (Figure 6i) and does not change under subsequent cycles.

The structure of the defect area is shown in **Figure 7**. We found that steps occur in the (112) plane and form locally a <111>/{112}-type twin structure. The newly formed twin

boundary has a low interfacial energy and it does not change much the energy balance after unloading. In addition, its high mobility helps the nanowire to recover its shape.

Seeding longer nanowires with conventional twin boundaries does indeed prevent dislocations from appearing and maintains a good shape recovery effect under repeated bending. We expect that seeding will also be possible for thicker nanowires, which is essential for potential applications.

2.5. The Driving Force for Pseudo-Elasticity

The formation of interfaces and deformation twinning induces permanent plastic strain in bulk crystals. Unlike their bulk counterparts, the pseudo-elasticity of nanowires is mediated by a reversible twinning mechanism.[15,17] The traditional understanding is that such pseudo-elastic behavior and shape recovery under tension is driven by the reduction of the surface energy.[14,15,17,18,39] The high surface energy of nanosized materials has even driven nanowires to undergo unusual martensitic phase transitions.[39,40] Here we will show that the scenario is quite different for bending deformations.

We analyze the driving forces during bending-induced pseudo-elasticity in terms of their energetics. The bending moment acting on the system will generate mechanical work. The mechanical work balances the changes of surface energy (ΔE_{sur}), the {110} interfaces (ΔE_{int}), and the elastic energy (ΔE_{ela}). We then calculate the components of ΔE_{sur}, ΔE_{int}, and ΔE_{ela} for the bending deformation in order to identify which part provides the primary driving force for the pseudo-elastic effect. **Figure 8**a shows a snapshot of the atomic configuration for the maximum bending angle $\theta = 80°$. The colors mark the potential energy per atom. The distribution of energies per atom in Figure 8b shows three regimes marked in blue
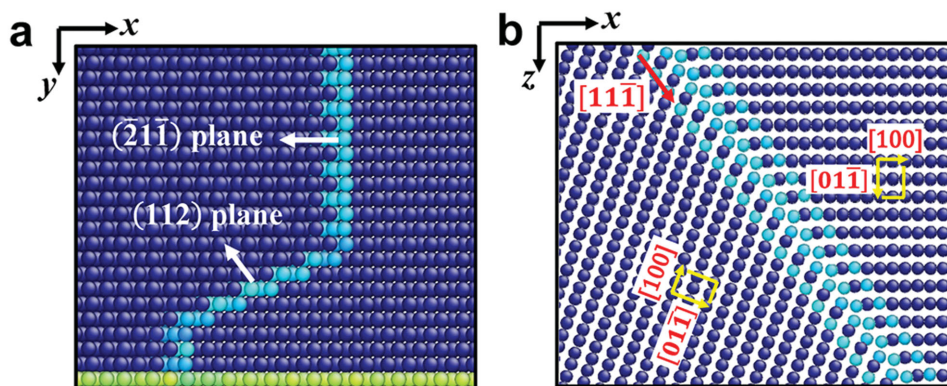
Figure 7. Structure of the step interface formed under unloading. a) Side view of the (112) interface, which is constructed by a series of <111>/{112} twin boundaries. b) Top view of the step interface in two atomic layers which consist of local <111>/{112} twins.

(elastic bulk energy), red (interfacial energy), and magenta (surface energy). No overlap exists between the surface energy and other energies so that it is straightforward to define atoms at the surface as those that have energies in the magenta regime. Some overlap exists between the elastic bulk energies and the interfacial energies. Most interfacial energies are well separated from elastic energies; these are atoms at the core of the interface. Atoms further away from the core approach the

bulk energy so that a limiting value was set to separate these two regimes. We determine the threshold between elastic and interfacial energy by the criterion that no isolated atoms in the bulk should contribute to the interface energy. This lower bound for the energy leads to a value for the threshold of -4.25 eV per atom. Typical energy distribution near the twin boundary is shown in Figure S2 (Supporting Information). The wider we choose the interfacial energy distribution
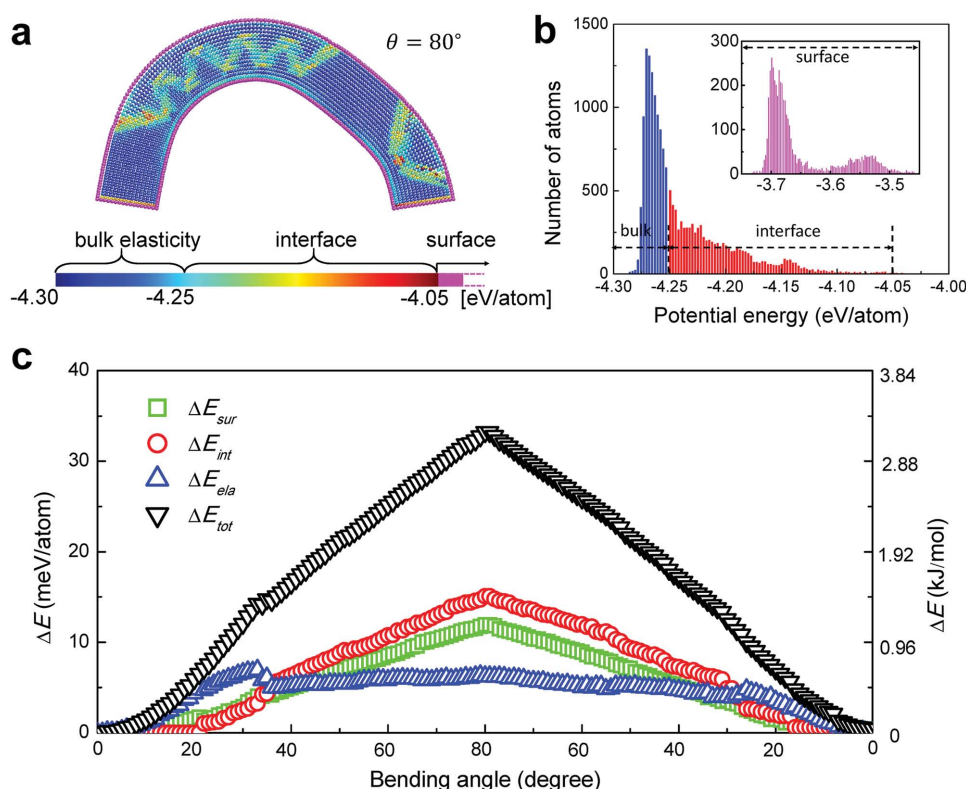

Figure 8. a) Distribution of potential energy in a bent nanowire at $\theta = 80°$ (shown in Figure 2f). The colors show the atomic potential energy for each atom. b) Distribution of atoms according to their potential energy. Three distinct energies are the elastic energy (blue), the interface energy (red), and the surface energy (magenta). Thresholds between the three groups were defined as -4.25 eV per atom (elastic to interfacial energy) and -4.05 eV per atom (interfacial to surface energy) c) Variation of energy components upon loading and unloading. Red circle, blue triangle, and green square represent ΔE_{int}, ΔE_{ela}, and ΔE_{sur}, separately. Black triangle represents the total potential energy as ΔE_{tot}. The {110} interfacial energy provides the main driving force for shape recovery.

FULL PAPER

the more atoms are counted as interfacial energy. As the total interfacial energy is dominated by its high energy tail, these small changes do not change the calculated energies in the three regimes very much. We then calculate the energy of each regime (the details are shown in Figure S3 in the Supporting Information), and then divide the energy by the total number of atoms in the nanowire so that the unit of energy becomes meV per atom. The resulting values of ΔE_{sur}, ΔE_{int}, and ΔE_{ela} for each bending angle are shown in Figure 8c during loading and unloading. Under loading, ΔE_{ela} increases during the elastic deformation and reaches a maximum at the end of the elastic regime near the lowest yield point. The elastic energy ΔE_{ela} remains almost unchanged in the subsequent plastic regime. ΔE_{sur} and ΔE_{int} do not change much during the elastic stage and increase gradually with increasing bending angle in the plastic regime. Comparing the magnitude of all components during detwinning, we find that ΔE_{int} is larger than the other energies in the plastic regime. The surface energy contributes little to small bending angles ($\theta < 32°$) and approaches the level of the elastic energy when the bending deformation is very large. During further unloading, all three components decrease, indicating that all contribute to the driving force for recovery. However, since the ΔE_{int} provides a large part of the three energy components, it also contributes greatly to the shape recovery. This result is quite different from pseudo-elasticity induced by tension, where surface energies provide the dominant driving force for shape recovery.[14,15]

2.6. Bending-Induced Twinning and Related Shape Recovery in Experiments

Deformation in bulk bcc metals at room temperature is usually controlled by dislocations with high lattice resistances.[28,41–46] However, in small-scale bcc crystals, the large surface area tends to destabilize bulk dislocation sources. As a result, nucleation of defects from the surface, including dislocations and twins, becomes a competing deformation mode at room temperature and low strain rates; twinning dominates when its nucleation from the surface is easier than that of dislocations. A recent experimental result shows twinning as the dominant deformation mechanism at nanoscale in bcc tungsten metal.[21] Our results are very similar.

The recent experiment in tungsten also shows that the competition between twinning and dislocations at the nanoscale still follows the Schmid law, indicating that the formation of twinning is orientation dependent.[21] Our simulations show that twinning occurs in the tensile regime with tension along [100] direction, which is again consistent with recent experimental work in tungsten.[21]

As for the bending pseudo-elasticity, there are very few experimental observations of shape recovery of bent nanowires. Previous experiments have shown that materials with almost "defect-free" structures can sustain large bending deformations, such as Cu,[47] GaP whiskers,[48] or Si nanowires.[49] It was argued that planar defects, such as stacking faults or twin boundaries, were generated upon bending, and shape recovery depends on the migration of defects. Our simulations show a similar effect where the role of defects is taken by the nucleation

and propagation of nonconventional interfaces along {110}. Similar interface driven shape recovery was observed in bulk Cu-Al-Ni SMAs with a triangle shaped twin morphology.[50] The crystallography of domain wall bending motions was elucidated in a multi-domain bar of In-Tl alloys.[51] For non-SMAs, highly localized twin bands were observed in magnesium alloy under three-point bending.[52]

3. Conclusion

Using atomistic simulations, we found shape recovery in bent [100]-oriented α-Fe nanowires. A nonconventional {110} interface is formed by piling up {112} local twin and <111>a/6 partial dislocations due to the stress gradient produced by bending. The {110} interface processes a high interfacial energy, and provides the primary driving force for shape recovery upon unloading. Such bending pseudo-elasticity can be extended to a wide range of wire diameters, if the sample is seeded with conventional twin boundaries which will transform to the desired {110} interfaces under bending.

4. Experimental Section

The atomic interactions in α-Fe were simulated by the embedded atom method (EAM).[53,54] The nanowire with an orientation of x-[100], y-[011], z-[0$\bar{1}\bar{1}$] and a simulation box of $80a \times 8\sqrt{2}\,a \times 8\sqrt{2}a$ (corresponding to 22.6 nm × 3.2 nm × 3.2 nm) were constructed, where a (=0.2855 nm) is the lattice repetition unit of α-Fe at 0 K. Before bending, the nanowire was relaxed at 300 K for 0.1 nanosecond using a Nosé–Hoover thermostat.[55,56] One atomic layer at both ends of the nanowire was fixed rigidly as the loading grip during bending. The bending was achieved by tilting the rigid loading ends against each other. The tilt was increased stepwise by $\Delta\theta = 1°$ per step and relaxed at 300 K for 0.1 nanosecond. Unloading experiments are performed in a similar way by reducing the tilt angle. The MD calculations were carried out in a canonical ensemble by using the large-scale atomic/molecular massively parallel simulator (LAMMPS) code,[57] and the atomic configurations were displayed by AtomEye.[58]

The generalized stacking fault energy, interstitial and vacancy formation energy, thermal expansion, and dislocation properties predicted by the potential[54] are in good agreement with density functional theory (DFT) calculations.[59,60] The potential was already used for the simulation of tensile and compressive deformation of α-Fe.[14,34–38,61,62] Previous simulations also showed that twinning is the dominant deformation mode for α-Fe nanowires under tension,[14,15,34–37,63] which is consistent with our simulations where twinning always nucleates from the tensile region of the sample under bending. The potential correctly predicted the sixfold core structure of screw dislocation as confirmed by DFT calculations.[64] We compile the properties calculated using our potential in Table S1 (Supporting Information) for comparison with experimental data.

Despite the good agreement between simulations and observations, one should not expect that semi-empirical potentials can reproduce all properties of the materials in full detail. To avoid errors due to deficiencies of the potential, we also used other potentials of α-Fe to check our simulation results.[65–68] The agreement between all potentials was very good (see Figure S4 in the Supporting Information). A further limitation of MD simulations of mechanical deformation lies in the high strain rate due to the short MD simulation time. To exclude possible effects induced by high strain rates, we also performed simulations using molecular statistics techniques, which is based on energy minimization by using the conjugate gradient algorithm and is independent of strain rate. The molecular statics simulations produced very similar results

FULL PAPER

as the MD simulations (Figure S5, Supporting Information). We expect that our potentials capture the essence of the nanostructure evolution of α-Fe, therefore.

Supporting Information

Supporting Information is available from the Wiley Online Library or from the author.

Acknowledgements

[1] S. S. P. Parkin, M. Hayashi, L. Thomas, *Science* **2008**, *320*, 190.
[2] U. Ruediger, J. Yu, S. Zhang, A. D. Kent, S. S. P. Parkin, *Phys. Rev. Lett.* **1998**, *80*, 5639.
[3] T. Phung, A. Pushp, C. Rettner, B. P. Hughes, S. H. Yang, S. S. P. Parkin, *Appl. Phys. Lett.* **2014**, *105*, 222404.
[4] A. Pushp, T. Phung, C. Rettner, B. P. Hughes, S. H. Yang, L. Thomas, S. S. P. Parkin, *Nat. Phys.* **2013**, *9*, 505.
[5] K. Otsuka, X. Ren, *Prog. Mater. Sci.* **2005**, *50*, 511.
[6] A. Planes, L. Manosa, *Solid State Phys.* **2001**, *55*, 159.
[7] X. D. Ding, T. Suzuki, X. B. Ren, J. Sun, K. Otsuka, *Phys. Rev. B* **2006**, *74*, 104111.
[8] T. Waitz, T. Antretter, F. D. Fischer, N. K. Simha, H. P. Karnthaler, *J. Mech. Phys. Solids* **2007**, *55*, 419.
[9] Y. Q. Fu, S. Zhang, M. J. Wu, W. M. Huang, H. J. Du, J. K. Luo, A. J. Flewitt, W. I. Milne, *Thin Solid Films* **2006**, *515*, 80.
[10] E. Salje, H. L. Zhang, *Phase Transit.* **2009**, *82*, 452.
[11] E. K. H. Salje, *ChemPhysChem* **2010**, *11*, 940.
[12] J. Novak, E. K. H. Salje, *J. Phys.: Condens. Mater.* **1998**, *10*, L359.
[13] J. K. Diao, K. Gall, M. L. Dunn, *Phys. Rev. B* **2004**, *70*, 075413.
[14] S. Z. Li, X. D. Ding, J. K. Deng, T. Lookman, J. Li, X. B. Ren, J. Sun, A. Saxena, *Phys. Rev. B* **2010**, *82*, 205435.
[15] S. Z. Li, X. D. Ding, J. Li, X. B. Ren, J. Sun, E. Ma, *Nano Lett.* **2010**, *10*, 1774.
[16] W. W. Liang, M. Zhou, *Phys. Rev. B* **2006**, *73*, 115409.
[17] W. W. Liang, M. Zhou, F. J. Ke, *Nano Lett.* **2005**, *5*, 2039.
[18] H. S. Park, K. Gall, J. A. Zimmerman, *Phys. Rev. Lett.* **2005**, *95*, 255504.
[19] H. S. Park, C. J. Ji, *Acta Mater.* **2006**, *54*, 2645.
[20] J. H. Seo, H. S. Park, Y. Yoo, T. Y. Seong, J. Li, J. P. Ahn, B. Kim, I. S. Choi, *Nano Lett.* **2013**, *13*, 5112.
[21] J. W. Wang, Z. Zeng, C. R. Weinberger, Z. Zhang, T. Zhu, S. X. Mao, *Nat. Mater.* **2015**, *14*, 594.
[22] C. L. Kelchner, S. Plimpton, J. Hamilton, *Phys. Rev. B* **1998**, *58*, 11085.
[23] E. K. H. Salje, *Phase Transitions in Ferroelastic and Co-elastic Crystals: An Introduction for Mineralogists, Material Scientists, and Physicists*, Cambridge University Press, Cambridge, UK **1990**.
[24] E. K. H. Salje, Y. Ishibashi, *J. Phys.: Condens Mater.* **1996**, *8*, 8477.
[25] B. H. Hong, S. C. Bae, C. W. Lee, S. Jeong, K. S. Kim, *Science* **2001**, *294*, 348.
[26] Z. Y. Huo, C. K. Tsung, W. Y. Huang, X. F. Zhang, P. D. Yang, *Nano Lett.* **2008**, *8*, 2041.
[27] J. R. Greer, W. D. Nix, *Phys. Rev. B* **2006**, *73*, 245410.
[28] J. P. Hirth, J. Lothe, *Theory of Dislocations*, Wiley, New York, NY, USA **1992**.
[29] M. D. Uchic, D. M. Dimiduk, J. N. Florando, W. D. Nix, *Science* **2004**, *305*, 986.
[30] J. R. Greer, W. C. Oliver, W. D. Nix, *Acta Mater.* **2005**, *53*, 1821.
[31] T. Zhu, J. Li, *Prog. Mater. Sci.* **2010**, *55*, 710.
[32] M. Chen, E. Ma, K. J. Hemker, H. Sheng, Y. Wang, X. Cheng, *Science* **2003**, *300*, 1275.
[33] Q. Yu, Z.-W. Shan, J. Li, X. Huang, L. Xiao, J. Sun, E. Ma, *Nature* **2010**, *463*, 335.
[34] A. Ojha, H. Sehitoglu, *Philos. Mag. Lett.* **2014**, *94*, 647.
[35] A. Ojha, H. Sehitoglu, L. Patriarca, H. J. Maier, *Modell. Simul. Mater. Sci. Eng.* **2014**, *22*, 075010.
[36] A. Ojha, H. Sehitoglu, L. Patriarca, H. J. Maier, *Philos. Mag.* **2014**, *94*, 1816.
[37] G. Sainath, B. K. Choudhary, T. Jayakumar, *Comput. Mater. Sci.* **2015**, *104*, 76.
[38] C. J. Healy, G. J. Ackland, *Acta Mater.* **2014**, *70*, 105.
[39] S. Z. Li, X. D. Ding, J. Li, X. B. Ren, J. Sun, E. Ma, T. Lookman, *Phys. Rev. B* **2010**, *81*, 245433.
[40] J. K. Diao, K. Gall, M. L. Dunn, *Nat. Mater.* **2003**, *2*, 656.
[41] J. Y. Kim, D. C. Jong, J. R. Greer, *Acta Mater.* **2010**, *58*, 2355.
[42] L. Huang, Q. J. Li, Z. W. Shan, J. Li, J. Sun, E. Ma, *Nat. Commun.* **2011**, *2*, 547.
[43] S. M. Han, G. Feng, J. Y. Jung, H. J. Jung, J. R. Groves, W. D. Nix, Y. Cui, *Appl. Phys. Lett.* **2013**, *102*, 041910.
[44] C. Marichal, H. Van Swygenhoven, S. Van Petegem, C. Borca, *Sci. Rep.* **2013**, *3*, 2547.
[45] K. Y. Xie, S. Shrestha, Y. Cao, P. J. Felfer, Y. B. Wang, X. Z. Liao, J. M. Cairney, S. P. Ringer, *Acta Mater.* **2013**, *61*, 439.
[46] C. Marichal, K. Srivastava, D. Weygand, S. Van Petegem, D. Grolimund, P. Gumbsch, H. Van Swygenhoven, *Phys. Rev. Lett.* **2014**, *113*, 025501.
[47] S. S. Brenner, C. R. Morelock, *Acta Metall. Mater.* **1956**, *4*, 89.
[48] E. Schönherr, E. Winckler, *J. Cryst. Growth* **1976**, *32*, 117.
[49] G. Stan, S. Krylyuk, A. Davydov, I. Levin, R. Cook, *Nano Lett.* **2012**, *12*, 2599.
[50] K. Otsuka, H. Sakamoto, K. Shimizu, *Scripta Metall. Mater.* **1977**, *11*, 41.
[51] H. D. Chopra, C. Bailly, M. Wuttig, *Acta Mater.* **1996**, *44*, 747.
[52] J. Baird, B. Li, S. Y. Parast, S. Horstemeyer, L. Hector, P. Wang, M. Horstemeyer, *Scr. Mater.* **2012**, *67*, 471.
[53] M. S. Daw, M. I. Baskes, *Phys. Rev. B* **1984**, *29*, 6443.
[54] M. I. Mendelev, S. Han, D. J. Srolovitz, G. J. Ackland, D. Y. Sun, M. Asta, *Philos. Mag.* **2003**, *83*, 3977.
[55] S. Nose, *J. Chem. Phys.* **1984**, *81*, 511.
[56] W. G. Hoover, *Phys. Rev. A* **1985**, *31*, 1695.
[57] S. Plimpton, *J. Comput. Phys.* **1995**, *117*, 1.
[58] J. Li, *Modell. Simul. Mater. Sci. Eng.* **2003**, *11*, 173.
[59] C. Bjorkas, K. Nordlund, *Nucl. Instrum. Meth. B* **2007**, *259*, 853.
[60] L. Malerba, M. C. Marinica, N. Anento, C. Bjorkas, H. Nguyen, C. Domain, F. Djurabekova, P. Olsson, K. Nordlund, A. Serra, D. Terentyev, F. Willaime, C. S. Becquart, *J. Nucl. Mater.* **2010**, *406*, 19.
[61] X. Tong, H. Zhang, D. Y. Li, *Sci. Rep.* **2015**, *5*, 8459.
[62] N. Gunkelmann, D. R. Tramontina, E. M. Bringa, H. M. Urbassek, *J. Appl. Phys.* **2015**, *117*, 085901.
[63] G. Sainath, V. S. Srinivasan, B. K. Choudhary, M. D. Mathew, T. Jayakumar, *AIP Conf. Proc.* **2014**, *1591*, 1182.
[64] C. Domain, G. Monnet, *Phys. Rev. Lett.* **2005**, *95*, 215506.
[65] S. L. Dudarev, P. M. Derlet, *J. Phys.: Condens. Mater.* **2005**, *17*, 7097.
[66] G. J. Ackland, D. J. Bacon, A. F. Calder, T. Harry, *Philos. Mag. A* **1997**, *75*, 713.
[67] G. J. Ackland, M. I. Mendelev, D. J. Srolovitz, S. Han, A. V. Barashev, *J. Phys.: Condens. Mater.* **2004**, *16*, S2629.
[68] M. I. Mendelev, S. W. Han, W. J. Son, G. J. Ackland, D. J. Srolovitz, *Phys. Rev. B* **2007**, *76*, 214105.